

Azimuthal Anisotropy Scaling Functions for Identified Particle and Anti-Particle Species across Beam Energies: Insights into Baryon Junction Effects

Roy A. Lacey^{1,*}

¹*Department of Chemistry, Stony Brook University,
Stony Brook, NY, 11794-3400, USA*

(Dated: December 10, 2024)

This study examines the beam energy dependence of azimuthal anisotropy scaling functions for mesons and baryons in Pb+Pb and Au+Au collisions across $\sqrt{s_{NN}} = 7.7$ GeV to 5.02 TeV. Species-dependent $v_2(p_T, \text{cent})$ measurements are used to derive scaling functions that unify anisotropy data across particle species, revealing the interplay between radial flow, hadronic re-scattering, and baryon junction effects. Results show that baryon junctions significantly enhance baryon v_n at low $\sqrt{s_{NN}}$, where the baryon chemical potential (μ_B) is high, driving a pronounced baryon-anti-baryon anisotropy difference. This difference diminishes with increasing $\sqrt{s_{NN}}$, reflecting the reduced influence of baryon junctions at higher energies. The non-monotonic behavior of the specific shear viscosity (η/s) and radial flow parameters for anti-baryons suggests a transition in expansion dynamics near $\sqrt{s_{NN}} = 39$ GeV, potentially linked to the QCD critical point. These findings provide new constraints on baryon transport mechanisms, baryon junction contributions, and the equation of state (EOS) and transport coefficients for baryon-rich matter.

PACS numbers: 25.75.-q, 25.75.Dw, 25.75.Ld

Azimuthal anisotropy measurements provide critical insights into the quark-gluon plasma (QGP) created in high-energy heavy-ion collisions by quantifying variations in particle emission relative to the reaction plane. These measurements are characterized by Fourier coefficients v_n , which encode the strength of anisotropic emission patterns [1, 2]. The v_n coefficients are sensitive to both the initial collision geometry and the QGP's transport properties, offering a robust probe of the medium's dynamics.

The azimuthal particle distribution is expressed via a Fourier expansion:

$$E \frac{d^3N}{dp^3} = \frac{1}{2\pi} \frac{d^2N}{p_T dp_T dy} \left(1 + 2 \sum_{n=1}^{\infty} v_n \cos[n(\phi - \Psi_n)] \right),$$

where ϕ is the particle's azimuthal angle relative to the n -th order event plane Ψ_n . The coefficients v_n represent azimuthal anisotropy in the n -th harmonic, arising from collective flow at low transverse momentum (p_T) or jet quenching at higher p_T .

At low transverse momentum (p_T), dominated by collective flow, the v_n coefficients arise from the conversion of initial spatial anisotropies into momentum-space anisotropies via strong pressure gradients [3, 4]. These coefficients are sensitive to transport properties such as the specific shear viscosity (η/s) and provide valuable insights into the equation of state (EOS), including its stiffness, which governs the efficiency of pressure gradients in driving expansion. Measurements of v_n across harmonic orders and particle species are essential for understanding the QGP's collective dynamics.

At higher transverse momentum (p_T), where jet quenching dominates, the v_n coefficients reflect the azimuthal dependence of parton energy loss as high-energy partons traverse the QGP [5–7]. This energy loss depends on the parton's path length (L) and the local medium density, quantified by the jet-quenching transport coefficient \hat{q} . Unlike flow-driven

anisotropy, high- p_T anisotropy arises from the differential energy loss of partons along trajectories relative to the reaction plane. Partons traveling out-of-plane experience longer path lengths and greater energy loss than those traveling in-plane. This path length difference (ΔL) drives the azimuthal anisotropy at high p_T , linking the collision geometry to directional energy loss. Examining the transition between flow- and jet-quenching-dominated regions provides key insights into the interplay between η/s and \hat{q} [8, 9].

The azimuthal anisotropy scaling function unifies $v_2(p_T, \text{cent})$ and $v_3(p_T, \text{cent})$ measurements into a single coherent framework, encapsulating parameters such as initial-state eccentricities (ε_n), dimensionless system size ($R \propto RT$), radial flow magnitude, stopping power (\hat{q}), specific shear viscosity ($\eta/s \propto T^3/\hat{q}$), and viscous corrections to the thermal distribution function (δ_f) [10, 11]. This framework effectively unifies data across systems and energies [8], enabling the simultaneous study of flow-driven anisotropy at low p_T and energy-loss-driven anisotropy at high p_T . A prior study for charged hadrons [8] has placed critical constraints on η/s , \hat{q} , and the eccentricity spectrum.

For a given system and centrality, the initial-state eccentricity and QGP transport properties, such as η/s , remain consistent across all particle species. Differences in $v_n(p_T, \text{cent})$ between species reflect their unique responses to radial flow and hadronic re-scattering. Radial flow, driven by pressure gradients, imparts a mass-dependent “blue shift” in $v_n(p_T)$, with heavier particles receiving a larger momentum boost due to greater inertia. This mass ordering of $v_n(p_T)$ is most pronounced at low to intermediate p_T and is amplified by a stiffer EOS with a higher pressure-to-energy density ratio, particularly benefiting baryons.

During the hadronic phase, hadronic re-scattering affects particle species based on their interaction cross-sections. Mesons and baryons, with differing cross-sections, undergo

varying degrees of re-scattering, with larger cross-sections leading to more significant interactions. This re-scattering modifies the final $v_n(p_T)$ and radial flow of particles and influences the effective specific shear viscosity (η/s), which reflects collective behavior in both the QGP and hadronic phases. Consequently, hadronic re-scattering plays a critical role in shaping anisotropic flow and the medium's transport properties.

Species-dependent $v_n(p_T, \text{cent})$ measurements disentangle the effects of radial flow and hadronic re-scattering, enabling precise constraints on the EOS and transport properties of the QGP. Recent work [9] has used $v_2(p_T, \text{cent})$ and $v_3(p_T, \text{cent})$ measurements for mesons and baryons to construct scaling functions, yielding deeper insights into radial flow and re-scattering effects while refining constraints on η/s , \hat{q} , and the eccentricity spectrum.

Beyond radial flow and hadronic re-scattering, baryon junctions are expected to significantly influence v_n differences between particles and anti-particles, particularly for baryons at lower beam energies where the baryon chemical potential (μ_B) is high. As topological configurations in QCD, baryon junctions enhance baryon stopping by transporting baryon number from forward and backward rapidity regions to mid-rapidity [12–16]. While string dynamics can also drive baryon stopping and increase mid-rapidity baryon densities [17], baryon junctions directly impact baryon transport through QCD topology, uniquely creating asymmetric baryon number distributions. This makes them a compelling mechanism for explaining the observed baryon–anti-baryon anisotropy differences at low beam energies.

Enhanced baryon stopping at mid-rapidity strengthens pressure gradients, modifying the collective dynamics of both the QGP and the hadronic phases. Since baryon stopping scales with μ_B , higher μ_B results in greater stopping and increased baryon densities. This effect amplifies baryon $v_n(p_T, \text{cent})$ relative to mesons and anti-baryons, particularly at low to intermediate p_T . While baryon junctions primarily drive the baryon–anti-baryon v_n difference, they also indirectly influence meson–anti-meson v_n differences by altering the quark–antiquark asymmetry and pressure gradients. Species-dependent v_n differences thus serve as a valuable tool to probe baryon junctions and their interplay with radial flow and hadronic re-scattering, providing insights into the EOS and transport properties of the medium.

At lower beam energies, elevated baryon chemical potential (μ_B) amplifies pressure gradients, disproportionately affecting baryons due to enhanced stopping, which increases their v_n relative to mesons and anti-baryons. Enhanced stopping directs momentum toward anisotropic flow, reducing the overall blue shift for baryons compared to mesons and anti-baryons. This distinction in radial flow between baryons and anti-baryons at the same centrality is critical for disentangling baryon stopping effects from general radial flow. Baryon junctions primarily enhance baryon stopping rather than uniformly increasing radial flow. At higher beam energies, where μ_B is small, baryon junction effects diminish, reducing stopping

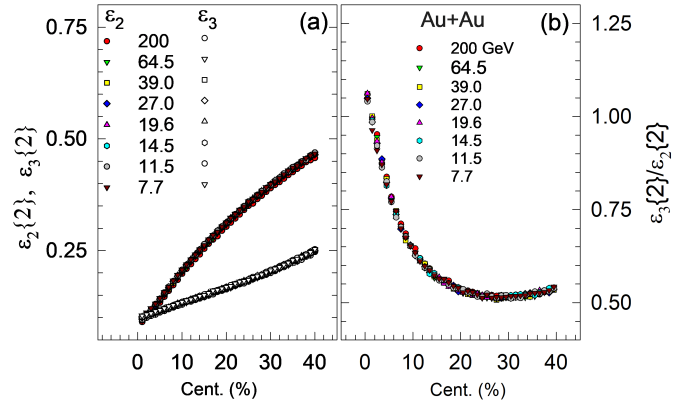


FIG. 1. (Color Online) Panel (a) shows the centrality-dependent values of $\varepsilon_2(\text{cent})$ and $\varepsilon_3(\text{cent})$ for Au+Au collisions at different beam energies. Panel (b) compares the $\varepsilon_3/\varepsilon_2$ ratios across beam energies, highlighting centrality and energy-dependent variations.

and making v_n more comparable between baryons and anti-baryons. This energy dependence provides a key probe of baryon transport mechanisms.

Extending the scaling framework to species-dependent $v_n(p_T, \text{cent})$ for baryons, mesons, particles, and anti-particles across beam energies enables the estimation of baryon junction contributions, providing insights into the evolution of radial flow, baryon transport, and the equation of state (EOS).

This study investigates scaling functions derived from species-dependent $v_n(p_T, \text{cent})$ measurements in Pb+Pb collisions at $\sqrt{s_{NN}} = 2.76$ and 5.02 TeV, and Au+Au collisions spanning $\sqrt{s_{NN}} = 7.7 - 200$ GeV. The analysis explores $v_n(p_T, \text{cent})$ scaling for particles and anti-particles to trace baryon junction effects and their energy dependence, incorporating the evolution of transport coefficients, hadronic re-scattering, and radial flow. These results provide insights into baryon transport and the evolution of medium properties with beam energy, offering a framework for understanding baryon stopping, baryon-rich QGP environments, and constraints on the equation of state (EOS).

The scaling functions are constructed using established principles for charged hadrons and identified particle species [8, 9], incorporating key parameters such as initial-state eccentricities (ε_n), dimensionless system size ($\mathbb{R} \propto \langle N_{\text{chg}} \rangle_{|y| \leq 0.5}^{1/3}$), radial flow magnitude, medium stopping power (\hat{q}), and specific shear viscosity ($\eta/s \propto T^3/\hat{q}$). The viscous correction to the thermal distribution function (δ_f) was applied using $\kappa = 0.17$ (GeV/c) $^{-2}$ [10, 11, 21]. Centrality-dependent charged-particle multiplicities $\langle N_{\text{chg}} \rangle_{|y| \leq 0.5}$ were taken from multiplicity density measurements [22–26].

Eccentricities were determined using the Monte Carlo quark-Glauber model (MC-qGlauber) [21], an extension of the standard MC-Glauber framework [27, 28] that incorporates quark substructure, quark distributions within nucleons, and cross sections consistent with nucleon-nucleon inelastic collisions at various beam energies. This model accounts for

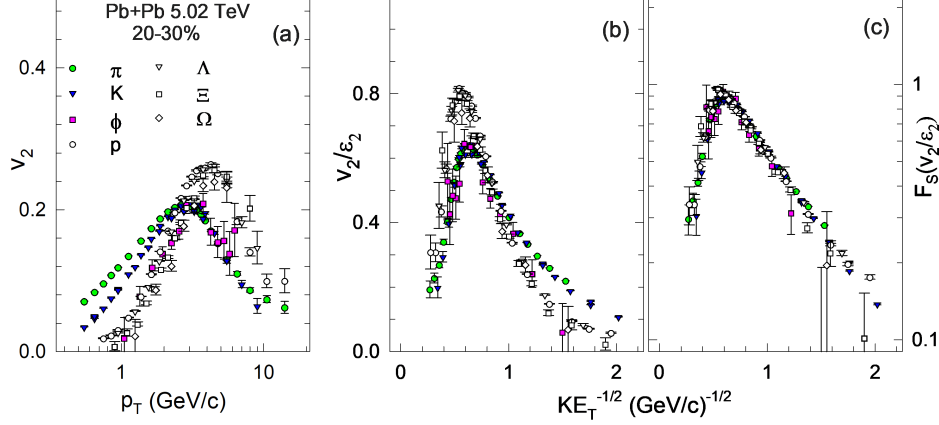


FIG. 2. (Color Online) Panel (a) compares $v_2(p_T)$ for mesons ($\pi^\pm, K^\pm, K_S^0, \phi$) and baryons ($p, \Lambda^0, \Xi^\pm, \Omega^\pm$), including anti-particles. Panel (b) shows eccentricity-scaled values (v_2/ε_2), while panel (c) displays the final scaling function for 20-30% central Pb+Pb collisions at $\sqrt{s_{NN}} = 5.02$ TeV. Data are from the ALICE collaboration [18–20].

the finite size of nucleons and their wounding profiles, with simulations for Au and Pb nuclei at their respective energies. The estimated systematic uncertainty for eccentricity values is 2-3%, attributed to model parameter variations. Selected eccentricities ($\varepsilon_{2,3}\{2\}$) for Pb+Pb collisions are detailed in Ref. [8]. Figure 1 compares $\varepsilon_{2,3}\{2\}$ values and their ratios across beam energies for Au+Au collisions, highlighting strong centrality dependence with minimal beam-energy variation.

Data for this study were obtained from the ALICE, PHENIX, and STAR collaborations, including $v_2(p_T, \text{cent})$ measurements for identified mesons ($\pi^\pm, K^\pm, K_S^0, \phi$) and baryons (${}^3\text{He}, d, p, \Lambda^0, \Xi^-, \Omega^-$), along with their antiparticles. These datasets provide a comprehensive basis for investigating azimuthal anisotropy across diverse particle species and collision energies.

Scaling functions were derived for the 20-30% centrality range in Pb+Pb collisions at $\sqrt{s_{NN}} = 2.76$ TeV [29–32] and 5.02 TeV [18–20], and for the 10-40% range in Au+Au collisions across $\sqrt{s_{NN}} = 7.7\text{--}200$ GeV [33–36]. Despite differing centrality ranges, the average centrality is comparable, ensuring consistent scaling comparisons. For Pb+Pb collisions at both beam energies and Au+Au collisions at $\sqrt{s_{NN}} = 200$ GeV, v_n values are averaged over particles and antiparticles due to negligible differences within measurement uncertainties. However, no averaging was applied for Au+Au at lower beam energies (7.7–62.4 GeV), where baryon stopping and baryon–antibaryon differences are more significant.

Minimal particle-antiparticle v_n differences at higher energies (Pb+Pb at both energies and Au+Au at 200 GeV) reflect the diminished baryon stopping and baryon junction effects, which result in a small baryon chemical potential (μ_B). Consequently, v_n values for baryons, anti-baryons, mesons, and anti-mesons are nearly identical at these energies. At lower beam energies, where baryon stopping and baryon junction effects are more pronounced, μ_B becomes larger, leading to sig-

nificant baryon–antibaryon v_n differences and smaller meson–antimeson differences. These patterns provide insights into baryon transport, baryon junctions, and QGP evolution across beam energies.

Mesons (M) and baryons (B), along with their anti-particles, were scaled separately to account for species-specific responses. The $v'_2(p_T, \text{cent})$ coefficients for K^+ in 5.02 TeV Pb+Pb collisions were used as the baseline for assessing hadronic re-scattering and radial flow effects. K^+ mesons, with their intermediate mass, are more sensitive to radial flow than lighter mesons like pions and interact less with the hadronic medium, providing a clean reference for hadronic re-scattering. Comparing K^+ with baryons of varying interaction cross-sections offers further insights into re-scattering effects.

For a given system at fixed centrality, hadronic re-scattering is estimated by scaling the $v''_{2,3}(p_T, \text{cent})$ coefficients for pions to the baseline:

$$\frac{v'_n(p_T)}{\varepsilon'_n} e^{\frac{n\beta'}{\varepsilon_0} [n+\kappa p_T^2] (\frac{\varepsilon_0}{\varepsilon'} - 1)} = \left(\frac{v''_n(p_T)}{\varepsilon''_n} \right)^{\zeta_M} e^{\frac{n\beta' \zeta_M}{\varepsilon_0} [n+\kappa p_T^2] (\frac{\varepsilon_0}{\varepsilon'} - 1)}, \quad (1)$$

and

$$\frac{v'_n(p_T, \text{cent})}{\varepsilon'_2(\text{cent})} e^{\frac{2n\beta'}{\varepsilon_0}} = \left(\frac{v_3(p_T, \text{cent})}{\varepsilon_3(\text{cent})} \right)^{\frac{2}{3} \zeta_M}. \quad (2)$$

Here, β' represents the specific shear viscosity (η/s) for the baseline, $\zeta_M = (1 - \zeta_{\text{hs}})$, and ζ_{hs} captures differences in hadronic re-scattering. The parameter α is a system-dependent normalization constant primarily tied to $\beta \propto \eta/s$.

Radial flow is estimated by scaling the $v'''_{2,3}(p_T, \text{cent})$ coefficients for baryons to the baseline:

$$\frac{v'_n(p_T)}{\varepsilon'_n} e^{\frac{n\beta'}{\varepsilon_0} [n+\kappa p_T^2] (\frac{\varepsilon_0}{\varepsilon'} - 1)} = e^{-n\beta' \zeta_B \frac{2\beta'}{\alpha \varepsilon_0}} \left(\frac{v'''_n(p_T)}{\varepsilon'''_n} \right)^{\zeta_B} e^{\frac{n\beta' \zeta_B}{\varepsilon_0} [n+\kappa p_T^2] (\frac{\varepsilon_0}{\varepsilon'} - 1)}, \quad (3)$$

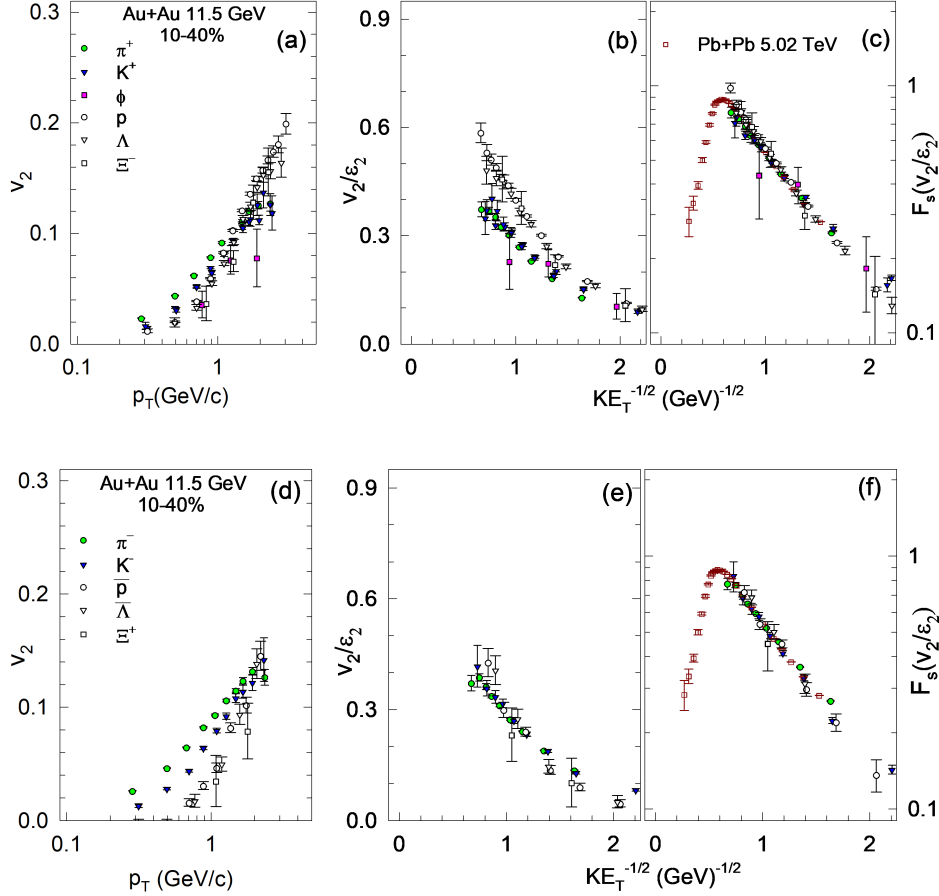


FIG. 3. (Color Online) Top panels (a-c) present $v_2(p_T)$, eccentricity-scaled values (v_2/ε_2), and scaling functions for identified particles in 10-40% central Au+Au collisions at $\sqrt{s_{NN}} = 11.5$ GeV. Bottom panels (d-f) show corresponding results for anti-particles. The scaling function for 20-30% central Pb+Pb collisions at 5.02 TeV is included for comparison. Data are from the STAR [33] and ALICE [18, 20] collaborations.

and

$$\frac{v'_2(p_T, \text{cent})}{\varepsilon'_2(\text{cent})} e^{\frac{2\alpha\beta'}{\varepsilon_0}} = e^{-2n_B\zeta_B \frac{2\alpha\beta}{\varepsilon_0}} \left(\frac{v_3(p_T, \text{cent})}{\varepsilon_3(\text{cent})} \right)^{\frac{2}{3}\zeta_B}. \quad (4)$$

Here, n_B is the baryon number, and $\zeta_B = (1 - \zeta_{\text{rf}}^B)^{n_B}$ for baryons or $(1 - \zeta_{\text{rf}}^{\bar{B}})^{n_B}$ for anti-baryons. The parameters ζ_{rf}^B and $\zeta_{\text{rf}}^{\bar{B}}$ represent species-specific differences in radial flow relative to the baseline.

The scaled difference in radial flow response between anti-baryons and baryons, $\Delta\zeta_{\text{rf}} = (\zeta_{\text{rf}}^{\bar{B}} - \zeta_{\text{rf}}^B)/\zeta_{\text{rf}}^{\bar{B}}$, estimates the influence of baryon junctions on baryon anisotropy, effectively separating junction effects from the blue shift caused by radial flow.

To improve scaling precision, KE_T -based scaling is employed, where transverse kinetic energy is defined as $\text{KE}_T = \left(\sqrt{p_T^2 + m_0^2} - m_0 \right)$, with m_0 being the particle's rest mass. This approach minimizes mass-dependent effects, enabling more accurate comparisons of anisotropy across different particle species [9].

Monitoring $\Delta\zeta_{\text{rf}}$ as a function of beam energy highlights

the onset and magnitude of baryon junction effects, offering insights into their implications for the equation of state.

The framework outlined in Eqs. 1–4 provides a systematic approach for assessing species-specific responses to radial flow and hadronic re-scattering, advancing the understanding of baryon junctions and their impact on the equation of state for baryon-rich matter.

Figure 2 demonstrates the scaling procedure for 20-30% central Pb+Pb collisions at 5.02 TeV. Panels (b) and (c) use $1/\sqrt{\text{KE}_T}$ on the x-axis to distinguish flow- and jet-quenching-dominated regions [37, 38]. Panel (a) highlights species-dependent differences in $v_2(p_T)$, while panel (b) shows that eccentricity scaling [$v_n(p_T)/\varepsilon_n$] combined with KE_T scaling improves agreement between mesons and baryons. Panel (c) presents the final scaling function, illustrating data convergence when blue shift effects are accounted for.

Figures 3 and 4 show the scaling procedure for 10-40% central Au+Au collisions at 11.5 and 27 GeV, respectively. Panels (a–c) present results for particles, and panels (d–f) show corresponding results for anti-particles. Panels (b), (c), (e), and (f) use $1/\sqrt{\text{KE}_T}$ on the x-axis to emphasize flow-

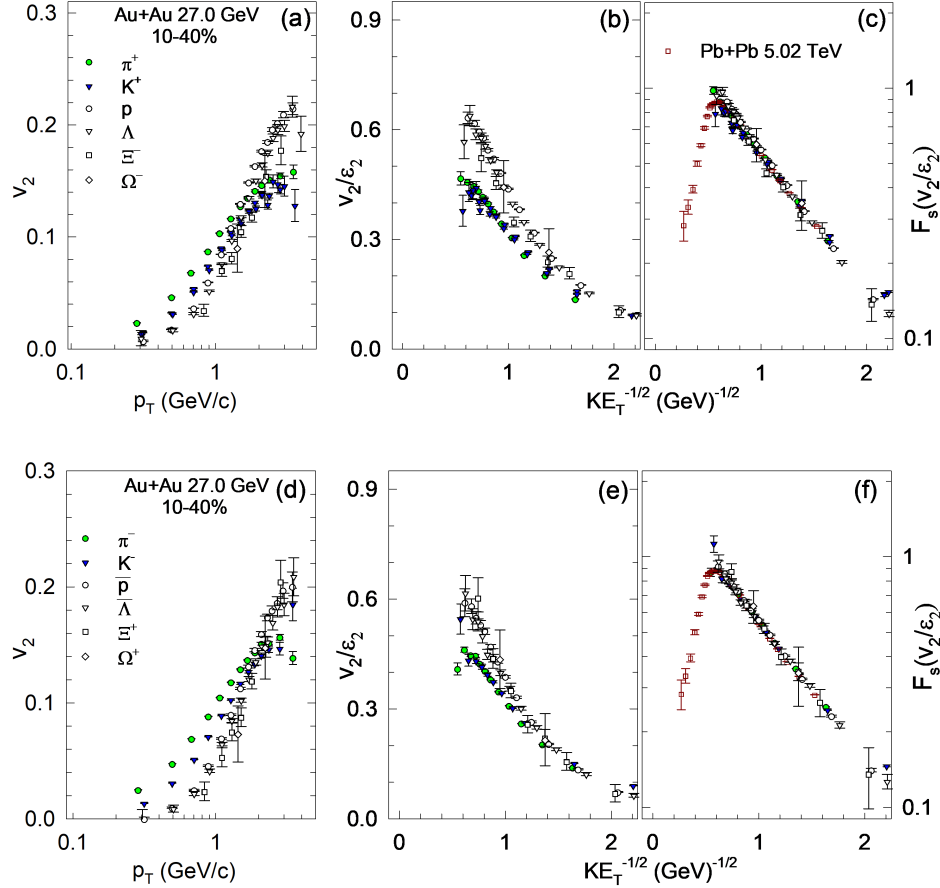


FIG. 4. (Color Online) Top panels (a-c) present $v_2(p_T)$, eccentricity-scaled values (v_2/ε_2), and scaling functions for identified particles in 10-40% central Au+Au collisions at $\sqrt{s_{NN}} = 27.0$ GeV. Bottom panels (d-f) show corresponding results for anti-particles. For comparison, the scaling function for 20-30% central Pb+Pb collisions at 5.02 TeV is included. Data are from the STAR [33] and ALICE [18, 20] collaborations.

and jet-quenching-dominated regions [37, 38]. Panels (a) and (d) illustrate species-dependent $v_2(p_T)$ differences, including particle–anti-particle comparisons. Panels (b) and (e) reveal that eccentricity scaling [$v_2(p_T)/\varepsilon_2$] and KE_T scaling enhance agreement between species, particularly for baryons and mesons, while highlighting species-dependent blue shift differences consistent with baryon junction effects. Panels (c) and (f) show the final scaling functions, with data converging onto a single curve. The scaling function for 20-30% central Pb+Pb collisions at 5.02 TeV is included for comparison. Scaling coefficients for Pb+Pb collisions ($\alpha = 1$, $\beta' = 0.88$, $\zeta_{hs} = 0.00$, $\zeta_{rf} = 0.390$) indicate minimal hadronic re-scattering and dominant QGP effects. In contrast, coefficients for Au+Au collisions at 11.5 GeV ($\alpha = 1.42$, $\beta = 0.62$, $\zeta_{hs} = 0.08$, $\zeta_{rf}^B = 0.01$, $\zeta_{rf}^{\bar{B}} = 0.290$) reflect substantial hadronic re-scattering, reduced radial flow, and effective η/s contributions from both QGP and hadronic phases. The high value of $\Delta\zeta_{rf}^B = 0.965$ further underscores significant baryon junction effects.

Scaling patterns for Au+Au collisions at 27 GeV (Fig. 4) are similar to those at 11.5 GeV (Fig. 3). However, panels (b)

and (e) show a reduced blue shift difference between baryons and anti-baryons, reflecting the weakening of baryon junction effects with increasing beam energy. Scaling coefficients ($\alpha = 1.59$, $\beta = 0.55$, $\zeta_{hs} = 0.065$, $\zeta_{rf}^B = 0.05$, $\zeta_{rf}^{\bar{B}} = 0.195$) indicate that higher beam energies reduce the impact of hadronic re-scattering, radial flow, η/s , and baryon junction contributions between 11.5 and 27 GeV.

Scaling functions were evaluated across the full range of beam energies to analyze the evolution of key scaling coefficients. Figure 5 highlights trends for hadronic re-scattering (ζ_{hs}) and the effective specific shear viscosity (β_{eff}). Panel (a) shows a monotonic decrease in ζ_{hs} with increasing beam energy, indicating reduced significance of hadronic re-scattering at higher energies. In contrast, panel (b) reveals a non-monotonic behavior of β_{eff} , suggesting a minimum in the effective η/s as beam energy decreases from 5.02 TeV to 39 GeV, followed by a sharp increase at 7.7 GeV. The initial drop in η/s may reflect more efficient QGP expansion at intermediate energies, potentially linked to the temperature dependence of η/s [39, 40]. This trend is consistent with changes in expansion dynamics influenced by the critical point of the QCD

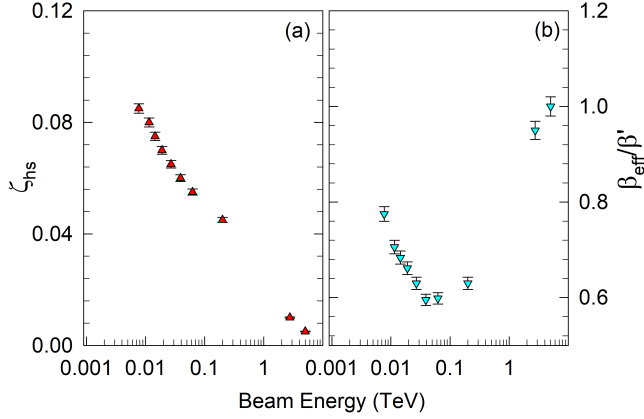


FIG. 5. (Color Online) Beam energy dependence of hadronic re-scattering parameter ζ_{hs} (panel a) and effective specific shear viscosity parameter β_{eff} , normalized to the Pb+Pb value at $\sqrt{s_{NN}} = 5.02$ TeV, β' (panel b). Results are from 20-30% central Pb+Pb collisions at $\sqrt{s_{NN}} = 2.76$ and 5.02 TeV and 10-40% central Au+Au collisions from $\sqrt{s_{NN}} = 7.7$ –200 GeV. Data from ALICE, PHENIX, and STAR collaborations [18–20, 29–36].

phase diagram. The subsequent rise in η/s at lower energies likely reflects enhanced hadronic re-scattering contributions, which impede expansion [41]. To enable consistent comparisons, β_{eff} is normalized to its value for Pb+Pb collisions at 5.02 TeV.

A non-monotonic trend is observed for the radial flow parameter of anti-baryons, $\zeta_{\text{rf}}^{\bar{B}}$, contrasting with the monotonic increase for baryons, ζ_{rf}^B , as shown in Fig. 6(a). This behavior suggests a transition in expansion dynamics near 39 GeV, reflecting changes in the relative contributions of the QGP and hadronic phases. At lower beam energies, baryon junctions enhance baryon stopping, increasing mid-rapidity baryon densities and altering the medium’s collective behavior. These effects underpin the energy-dependent trends in ζ_{rf}^B and $\zeta_{\text{rf}}^{\bar{B}}$.

The non-monotonic trend in $\zeta_{\text{rf}}^{\bar{B}}$ also reflects the growing influence of the hadronic phase at lower beam energies, where hadronic re-scattering becomes more significant. Flow filtering further shapes this trend, as low-momentum anti-baryons are more susceptible to annihilation in the dense medium, leaving a higher-momentum population and amplifying the radial flow signal. This interplay between baryon junction effects, hadronic re-scattering, and flow filtering results in a pronounced anisotropy difference between baryons and anti-baryons.

The normalized difference $\Delta\zeta_{\text{rf}}$, shown in Fig. 6(b), highlights the increasing role of baryon junctions at $\sqrt{s_{NN}} < 62.4$ GeV. For higher energies ($\sqrt{s_{NN}} \geq 200$ GeV), $\Delta\zeta_{\text{rf}}$ approaches zero, reflecting diminished baryon junction effects. At lower energies, these junctions enhance baryon stopping, leading to higher baryon densities and greater anisotropy for baryons relative to anti-baryons. Mesons and anti-mesons, less influenced by baryon junctions, primarily reflect radial flow and hadronic re-scattering effects.

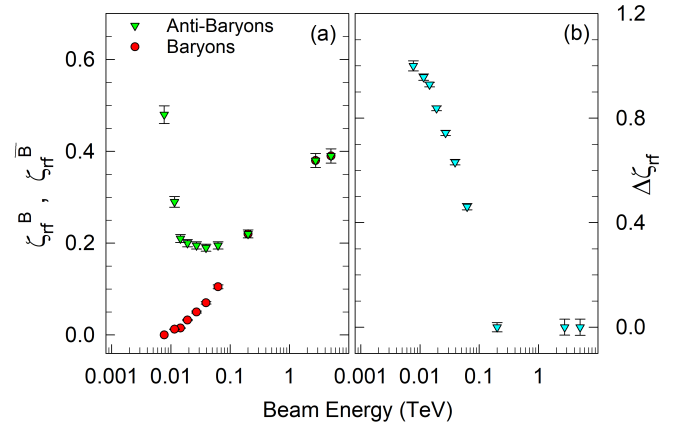


FIG. 6. (Color Online) Beam energy dependence of the radial flow parameters for baryons (ζ_{rf}^B) and anti-baryons ($\zeta_{\text{rf}}^{\bar{B}}$) (panel a), as well as their normalized difference $\Delta\zeta_{\text{rf}} = (\zeta_{\text{rf}}^{\bar{B}} - \zeta_{\text{rf}}^B)/\zeta_{\text{rf}}^B$, which provides an estimate of the influence of baryon junctions (panel b). The ζ_{rf} values are extracted from 20-30% central Pb+Pb collisions at $\sqrt{s_{NN}} = 2.76$ and 5.02 TeV, and from 10-40% central Au+Au collisions spanning the range $\sqrt{s_{NN}} = 7.7$ –200 GeV. Data are sourced from the ALICE, PHENIX, and STAR collaborations [18–20, 29–36].

The scaling patterns for mesons and baryons provide a systematic framework for studying species-dependent contributions of radial flow, hadronic re-scattering, and baryon junction effects. Mesons, less sensitive to baryon transport, primarily reflect the balance between radial flow and hadronic re-scattering. In contrast, baryons at lower beam energies are dominated by baryon junction effects, which govern their transport dynamics and anisotropic flow. This species-dependent behavior is essential for isolating baryon junction effects and investigating baryon stopping as a function of beam energy.

In summary, this study establishes a comprehensive framework for analyzing azimuthal anisotropy across beam energies, using scaling functions based on species-dependent measurements and key transport properties. The results reveal distinct responses to radial flow, hadronic re-scattering, and baryon junction effects, particularly the significant role of baryon junctions in baryon–anti-baryon anisotropy at lower beam energies. At higher energies, these effects diminish, yielding more similar $v_n(p_T, \text{cent})$ values for particles and anti-particles. The observed non-monotonic behavior in $\beta_{\text{eff}} \propto \eta/s$ and the radial flow parameter for anti-baryons suggests changes in expansion dynamics, potentially linked to the QCD critical point. These findings impose constraints on the equation of state and provide a robust methodology for future studies on baryon transport, hadronic re-scattering, and QGP evolution, offering deeper insights into the dynamics of baryon-rich environments.

* E-mail: Roy.Lacey@Stonybrook.edu

- [1] J.-Y. Ollitrault, *Phys. Rev.* **D46**, 229 (1992).
- [2] S. A. Voloshin, A. M. Poskanzer, and R. Snellings, *Landolt-Bornstein* **23**, 293 (2010), arXiv:0809.2949 [nucl-ex].
- [3] U. Heinz and R. Snellings, *Ann. Rev. Nucl. Part. Sci.* **63**, 123 (2013).
- [4] C. Gale, S. Jeon, and B. Schenke, *Int. J. Mod. Phys.* **A28**, 1340011 (2013).
- [5] J. D. Bjorken, (1982).
- [6] R. Baier, Y. L. Dokshitzer, A. H. Mueller, S. Peigne, and D. Schiff, *Nucl. Phys. B* **483**, 291 (1997), arXiv:hep-ph/9607355.
- [7] A. Majumder and C. Shen, *Phys. Rev. Lett.* **109**, 202301 (2012), arXiv:1103.0809 [hep-ph].
- [8] R. A. Lacey, *Phys. Rev. C* **110**, L031901 (2024), arXiv:2402.09389 [nucl-ex].
- [9] R. A. Lacey, (2024), arXiv:2410.04329 [nucl-ex].
- [10] A. Majumder, B. Muller, and X.-N. Wang, *Phys. Rev. Lett.* **99**, 192301 (2007), arXiv:hep-ph/0703082.
- [11] K. Dusling, G. D. Moore, and D. Teaney, *Phys. Rev. C* **81**, 034907 (2010), arXiv:0909.0754 [nucl-th].
- [12] D. Kharzeev, *Phys. Lett. B* **378**, 238 (1996), arXiv:nucl-th/9602027.
- [13] G. C. Rossi and G. Veneziano, *Nucl. Phys. B* **123**, 507 (1977).
- [14] S. E. Vance, M. Gyulassy, and X. N. Wang, *Phys. Lett. B* **443**, 45 (1998), arXiv:nucl-th/9806008.
- [15] N. Lewis, W. Lv, M. A. Ross, C. Y. Tsang, J. D. Brandenburg, Z.-W. Lin, R. Ma, Z. Tang, P. Tribedy, and Z. Xu, *Eur. Phys. J. C* **84**, 590 (2024), arXiv:2205.05685 [hep-ph].
- [16] N. Magdy, A. Deshpande, R. Lacey, W. Li, P. Tribedy, and Z. Xu, (2024), arXiv:2408.07131 [hep-ph].
- [17] S. Pratt, *Phys. Rev. C* **109**, 044910 (2024), arXiv:2311.17906 [hep-ph].
- [18] Y. Zhu (ALICE), *PoS ICHEP2018*, 441 (2019).
- [19] S. Acharya *et al.* (ALICE), *Phys. Rev. C* **102**, 055203 (2020), arXiv:2005.14639 [nucl-ex].
- [20] S. Acharya *et al.* (ALICE), *JHEP* **05**, 243 (2023), arXiv:2206.04587 [nucl-ex].
- [21] P. Liu and R. A. Lacey, *Phys. Rev. C* **98**, 021902 (2018), arXiv:1802.06595 [nucl-ex].
- [22] K. Aamodt *et al.* (ALICE), *Phys. Rev. Lett.* **106**, 032301 (2011), arXiv:1012.1657 [nucl-ex].
- [23] J. Adam *et al.* (ALICE), *Phys. Rev. Lett.* **116**, 222302 (2016), arXiv:1512.06104 [nucl-ex].
- [24] S. Acharya *et al.* (ALICE), *Phys. Lett. B* **790**, 35 (2019), arXiv:1805.04432 [nucl-ex].
- [25] A. M. Sirunyan *et al.* (CMS), *Phys. Lett. B* **799**, 135049 (2019), arXiv:1902.03603 [hep-ex].
- [26] R. A. Lacey, P. Liu, N. Magdy, M. Csanád, B. Schweid, N. N. Ajitanand, J. Alexander, and R. Pak, (2016), arXiv:1601.06001 [nucl-ex].
- [27] M. L. Miller, K. Reygers, S. J. Sanders, and P. Steinberg, *Ann. Rev. Nucl. Part. Sci.* **57**, 205 (2007), arXiv:nucl-ex/0701025.
- [28] B. Alver *et al.* (PHOBOS), *Phys. Rev. Lett.* **98**, 242302 (2007), arXiv:nucl-ex/0610037.
- [29] B. B. Abelev *et al.* (ALICE), *JHEP* **06**, 190 (2015), arXiv:1405.4632 [nucl-ex].
- [30] J. Adam *et al.* (ALICE), *JHEP* **09**, 164 (2016), arXiv:1606.06057 [nucl-ex].
- [31] S. Acharya *et al.* (ALICE), *Eur. Phys. J. C* **77**, 658 (2017), arXiv:1707.07304 [nucl-ex].
- [32] S. Acharya *et al.* (ALICE), *Phys. Lett. B* **784**, 82 (2018), arXiv:1805.01832 [nucl-ex].
- [33] L. Adamczyk *et al.* (STAR), *Phys. Rev. C* **88**, 014902 (2013), arXiv:1301.2348 [nucl-ex].
- [34] A. Adare *et al.* (PHENIX), *Phys. Rev. C* **93**, 051902 (2016), arXiv:1412.1038 [nucl-ex].
- [35] L. Adamczyk *et al.* (STAR), *Phys. Rev. Lett.* **116**, 062301 (2016), arXiv:1507.05247 [nucl-ex].
- [36] M. Abdallah *et al.* (STAR), *Phys. Rev. C* **105**, 064911 (2022), arXiv:2203.07204 [nucl-ex].
- [37] Y. L. Dokshitzer and D. E. Kharzeev, *Phys. Lett. B* **519**, 199 (2001), arXiv:hep-ph/0106202.
- [38] R. A. Lacey, A. Taranenko, R. Wei, N. Ajitanand, J. Alexander, *et al.*, *Phys. Rev. C* **82**, 034910 (2010), arXiv:1005.4979 [nucl-ex].
- [39] L. P. Csernai, J. I. Kapusta, and L. D. McLerran, *Phys. Rev. Lett.* **97**, 152303 (2006), arXiv:nucl-th/0604032.
- [40] R. A. Lacey, N. Ajitanand, J. Alexander, P. Chung, W. Holzmann, *et al.*, *Phys. Rev. Lett.* **98**, 092301 (2007), arXiv:nucl-ex/0609025 [nucl-ex].
- [41] T. Hirano, U. W. Heinz, D. Kharzeev, R. Lacey, and Y. Nara, *Phys. Lett. B* **636**, 299 (2006), arXiv:nucl-th/0511046 [nucl-th].